Journal of
Materials Chemistry C

Materials for optical, magnetic and electronic devices

Accepted Manuscript

This article can be cited before page numbers have been issued, to do this please use: E. Maggi, A. Navarro, O. Segura-Blanch, I. Caño Prades, L. Calvo-Barrio, L. Soler and E. Saucedo, *J. Mater. Chem. C*, 2026, DOI: 10.1039/D6TC00789A.

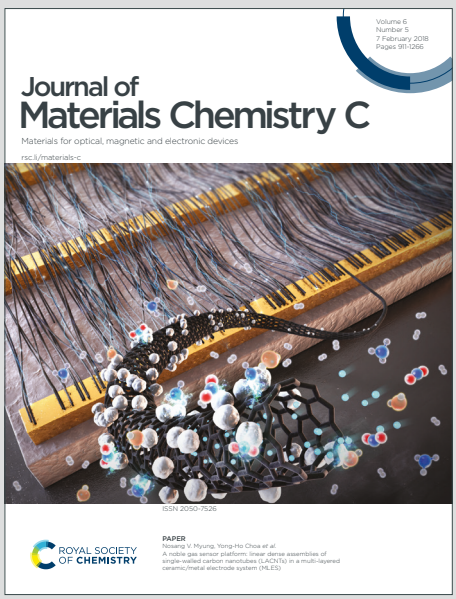

ROYAL SOCIETY OF CHEMISTRY

rsc.li/materials-c

View Article Online
DOI: 10.1039/D6TC00789A

Quasi-1D SbSeI as a Photocathode for Light-driven Hydrogen Production

Edoardo Maggi [a,b,c], Alejandro Navarro Güell [a], Ivan Caño [a,c], Oriol Segura-Blanch [a,c], Lorenzo Calvo-Barrio [d,e], Lluis Soler [b,c], Edgardo Saucedo [a,c]

[a] Micro and Nanotechnology Group, Emerging Thin Film Photovoltaics Lab, Universitat Politècnica de Catalunya (UPC), Barcelona, Spain. Email: edgardo.saucedo@upc.edu [b] Institute of Energy Technologies and Department of Chemical Engineering, Universitat Politècnica de Catalunya (UPC), Barcelona, Spain. Email: lluis.soler.turu@upc.edu [c] Barcelona Research Center in Multiscale Science and Engineering, Universitat Politècnica de Catalunya (UPC), Barcelona, Spain
[d] Centres Cientı´fics i Tecnolo`gics (CCiTUB), Universitat de Barcelona, Barcelona, Spain
[e] IN2UB, Departament d'Enginyeria Electro`nica i Biome`dica, Universitat de Barcelona, Barcelona, Spain

Abstract

This work reports the first functional implementation of SbSeI as a photocathode for photoelectrochemical hydrogen production via water splitting. SbSeI is a quasi-one-dimensional chalcohalide semiconductor that naturally forms nano/micro-ribbon structures, offering highly anisotropic charge transport and an increased interfacial surface area for photoelectrochemical reactions when properly oriented. Operating in neutral phosphate buffer, the SbSeI devices achieve a photocurrent density of 1.2 mA/cm², a half-cell solar-to-hydrogen efficiency of 0.4%, and an onset potential of 0.6 V_{RHE}. Stable hydrogen evolution is sustained under continuous operation, demonstrating the intrinsic robustness of the material system under working conditions. A comprehensive structural, morphological, and photoelectrochemical characterization is presented, elucidating how absorber morphology and interfacial engineering govern charge transfer, efficiency, and stability. Importantly, these performances are achieved using simple device architectures, neutral electrolytes, and without reliance on scarce or noble metal nanoparticle catalysts, highlighting SbSeI as a sustainable and promising photocathode material for solar-driven hydrogen production.

View Article Online
DOI: 10.1039/D6TC00789A

Introduction

The rapidly increasing global demand for renewable and sustainable energy has intensified efforts to develop clean technologies capable of addressing both environmental and energy-related challenges. Among these, photoelectrochemical (PEC) water splitting has emerged as a promising approach for solar-driven hydrogen (H_2) production, enabling the direct conversion of sunlight into chemical fuel using semiconductors as light absorbers. [1–5]

In PEC systems, photogenerated charge carriers extracted from a semiconductor drive the hydrogen evolution reaction (HER) and the oxygen evolution reaction (OER) at solid–liquid interfaces. For HER, the conduction band minimum (CBM) of the semiconductor must lie at a more cathodic potential than the H^+/H_2 redox level (−4.44 eV vs. vacuum), while OER requires the valence band maximum (VBM) to be positioned at a more anodic potential than the H_2O/O_2 redox level (−5.67 eV vs. vacuum).[6–8] In practice, however, kinetic limitations associated with interfacial charge transfer and multielectron reactions introduce additional overpotentials, thereby increasing the effective energetic requirements for an efficient PEC operation.[9]

In this context, quasi-one-dimensional (Q1D) van der Waals semiconductors have recently attracted growing interest as emerging candidates for energy conversion applications.[10] These materials combine low toxicity, non-critical raw material composition, and defect tolerance with a highly anisotropic crystal structure.[11] Unlike conventional three-dimensional semiconductors, many Q1D materials exhibit strong covalent bonding along one crystallographic direction and weak van der Waals interactions along the other two directions.[12] This pronounced anisotropy gives rise to ribbon-like nano/micro-structures with directional charge transport, improved light trapping, and reduced optical reflection. Additionally, in the context of PEC, their high surface area can facilitate electrolyte adsorption.[13]

To date, experimental reports on Sb(Bi)Se(S)I(Br) chalcohalides for HER and/or OER remain extremely limited. Only a few materials in this class, such as SbSI [14] and BiSI [15], have shown early signs of measurable PEC photoactivity. For the majority of chalcohalides no direct HER/OER performance metrics have yet been published. The existing literature comprises either photocatalytic degradation studies or theoretical predictions suggesting favourable band alignments for water splitting.[16]Among Q1D compounds, SbSeI represents a particularly compelling yet under-investigated material. Despite being among the most studied chalchohalides, effort in research has been mainly focussed towards a material synthesis/characterization perspective,[17–20] while its implementation in functional PEC devices remains unexplored. From an energetic standpoint, SbSeI exhibits a favourable band alignment for HER : its conduction band position (−4.01 eV vs. vacuum), (Fig.S1) provides sufficient driving force for proton reduction, even when accounting for kinetic overpotentials (~0.1 eV [9]). Simultaneously, its valence band position (−5.71 eV vs. vacuum) (Fig.S1) limits the energetic driving force for water oxidation at the photocathode–electrolyte interface, a possible cause of performance loss and instability in PEC photocathodes. [21]

Beyond intrinsic band energetics, morphology and surface chemistry can also play a decisive role in determining PEC performance. [22] Actually, in both photocatalysis (PC) and PEC, the overall reaction kinetics are often limited by interfacial charge-transfer and product desorption processes rather than by bulk charge generation/transfer. While photogenerated charges are formed on ultrafast timescales (femtoseconds) and charge transport/recombination typically occur in the picosecond to millisecond timescale, surface electrochemical reactions generally proceed more slowly, ranging from nanoseconds (oxidation or reduction involving trapped carriers) to milliseconds (product desorption).[23] Consequently, the morphology of the semiconductor layer in direct contact with the electrolyte plays a critical role in determining the PEC performance.

Moreover, to further decouple intrinsic material properties from degradation-related effects, surface and interface engineering strategies are also required. In this context, ultrathin protective layers represent an

View Article Online
DOI: 10.1039/D6TC00789A

effective approach to stabilize the semiconductor–electrolyte interface while preserving efficient charge transfer. When sufficiently thin, these layers can suppress direct contact between the absorber and the electrolyte, mitigate surface recombination, and enhance operational stability, while still allowing photogenerated carriers to tunnel to the electrolyte interface. [24] The thickness and electronic properties of such overlayers are critical, as excessive thickness or poor conductivity can introduce resistive losses and limit photocurrent extraction.

Here, we report the first functional SbSeI-based photocathodes for PEC HER. By systematically investigating the effects of absorber morphology, ultrathin TiO_2 passivation, and interfacial charge-transfer dynamics, we demonstrate how the unique Q1D structure of SbSeI can be leveraged to achieve stable and reproducible PEC performance even without the need for scarce and expensive noble nanoparticles. The high tunability of the columnar SbSeI structure is presented and exploited to investigate three distinct morphologies, aiming to balance photon absorption and reactant accessibility while avoiding excessive shadowing effects or product trapping phenomena that could hinder interfacial charge transfer. A detailed comparison between bare and protected SbSeI absorbers is presented, both in terms of photoelectrochemical behaviour and structural evolution. Photocurrent densities, half-cell solar to hydrogen (HC-STH) efficiencies, and onset potentials (V_{on}) have been studied for the different device configurations. To prioritize sustainability and future scalability, the PEC architecture and testing conditions were deliberately chosen to exclude acidic electrolytes and expensive or scarce nanoparticle catalysts, with all measurements performed in neutral phosphate buffer. The stability of the devices in operation under continuous bias and illumination was also assessed.

Experimental

Device fabrication

Fluorine-doped tin oxide (FTO) coated SLG (Soda Lime Glass) (Sigma-Aldrich, TEC 15) has been used as a conductive substrate. FTO was selected as the back contact due to its widespread use in PEC systems and its superior chemical stability in aqueous electrolytes. [25,26] Before the absorber deposition, substrates were subjected to a multistep cleaning protocol. This procedure consisted of an initial manual cleaning using deionized water and laboratory detergent (Liquinox), followed by sequential ultrasonic baths (10 min each) in isopropanol and Milli-Q water. Finally, the substrates were treated in an ozone cleaner for 10 min to remove residual organic contaminants and enhance surface wettability.

Sb_2Se_3 precursor layers were deposited using a co-evaporation system (Kenosistec 500 CK CLUSTER) operated at a base pressure of 5×10^{-7} mbar. The deposition sequence began with the evaporation of a thin Sb seed layer for 60 s (Sigma-Aldrich, 100 mesh, 99.5%) onto substrates maintained at 270 °C. Subsequently, Sb and Se (Thermo Scientific, 200 mesh, 99.999% purity) were co-evaporated to form a Sb_2Se_3 film with a target thickness of 500 nm. Upon completion of the deposition, the substrates were allowed to cool down naturally to 180 °C. During this cooling stage, Se evaporation was maintained in order to mitigate Se loss through re-evaporation from the freshly deposited film.

The conversion of Sb_2Se_3 into SbSeI was achieved via a thermal treatment conducted in a high-pressure furnace (MTI corporation). For this process, FTO/Sb_2Se_3 samples were placed inside a covered Petri dish together with 100 mg of SbI_3 powder (Thermo Scientific, 99.999% purity). The furnace temperature was increased at a controlled rate of 10 °C/min to the target final temperature. All the annealing processes were performed under an initial Ar pressure of 4.5 bar. Three different processes have been performed in order to vary the obtained morphology of the resultant SbSeI. For SbSeI(1) and SbSeI(2), the final temperature (isothermal hold) was set to 450 °C, and kept for 30 min and 1 min, respectively. For SbSeI(3), the final

View Article Online
DOI: 10.1039/D6TC00789A

temperature was set to 250 °C and kept for 60 min. In all the cases, the system was allowed to cool down naturally to room temperature.

Surface passivation of the SbSeI absorber was realized by depositing a thin TiO_2 layer via atomic layer deposition (ALD) using a Savannah S200 system (Cambridge NanoTech). Tetrakis(dimethylamino)titanium(IV) (TDMAT) and deionized water (resistivity 16 MΩ cm) were employed as the metal and oxidant precursors, respectively, while high-purity nitrogen (99.999%) served as both carrier and purge gas. The deposition was carried out at a chamber temperature of 120 °C and a pressure of 0.1 mbar to prevent SbSeI degradation. The pulse times for TDMAT, DI-H_2O, and the N_2 purge steps were 0.02 s, 0.8 s, and 0.02 s, respectively. The TiO_2 thickness was controlled by adjusting the number of ALD cycles, yielding final layer thicknesses of 3 nm or 10nm.

The completed devices were cleaved into ~1 cm^2 samples for electrochemical testing. The electrical contact was established by selectively scribing the upper layers to expose the underlying back contact. A copper wire was then attached using an indium solder, ensuring a low-resistance and a mechanically stable connection. To prevent an undesired electrolyte contact and parasitic illumination effects, the edges of each device were sealed using adhesive Teflon tape, leaving only the defined active area exposed to the electrolyte and the light source.

Characterization

The thickness and elemental composition of the Sb_2Se_3 and SbSeI films were routinely monitored after each deposition by X-ray fluorescence (XRF) spectroscopy (Fisherscope X-ray XDAL 237 SSD, 50kV, Ni10 filter) to confirm the Sb:Se:I atomic ratio of 1:1:1. Additional confirmation of the 1:1:1 stoichiometry is provided by energy-dispersive X-ray spectroscopy (EDX) reported in our previous work.[27]

Raman measurements were performed in backscattering geometry with a Renishaw inVia Qontor spectrometer equipped with a 532 nm laser source. To minimize laser-induced heating effects, the incident power was limited to 0.5 mW. Spectral calibration was carried out using the first-order Raman peak of monocrystalline silicon.

Structural characterization was conducted by X-ray diffraction (XRD) using a Bruker D8 Advance diffractometer operating in Bragg–Brentano configuration with Cu Kα radiation (λ = 1.54187 Å). Diffraction patterns were collected over a 2θ range from 20° to 80° with a step size of 0.01°, and the data were analyzed using the "X'Pert HighScore" software.

XPS (X-ray Photoelectron Spectroscopy), LEIPS (Low Energy Inverse Photoemission Spectroscopy) and LEET (Low Energy Electron Transmission) characterizations were performed in CCiTUB using ESFOSCAN, an equipment based on the PHI VersaProbe 4 instrument from Physical Electronics (ULVAC-PHI). XPS measurements were carried out using a monochromatic focused Al Kα X-ray source (1486.6 eV). The analysed area was a circular spot of 100 μm in diameter, and the energy resolution was set to 224 eV Pass Energy with 0.8 eV/step for survey spectra, and 27 eV Pass Energy with 0.1 eV/step for high resolution spectra. Measurements were performed using a Helium source (21.22 eV) calibrated using an Ag reference sample with a work function of 4.27 eV. The analysed area was approximately 1.5 mm in diameter, and the energy resolution was set to 1.3 eV Pass Energy with 0.01 eV/step. Spectra were acquired both with and without applying a negative bias voltage of approximately −10 V to the sample. The LEIPS spectra were performed with a 10 eV electron source incident on the sample with lower values because the support is biased while measuring, and a 4.22 eV bandpass filter higher than the expected electron affinities. All measurements were performed in an ultra-high vacuum (UHV) chamber at pressures between 5x10-10 and 5x10-9 Torr. Data analysis was performed using the MultiPak software (V. 9.9.2).

View Article Online
DOI: 10.1039/D6TC00789A

The morphological analysis was performed by scanning electron microscopy (SEM) using a Zeiss Auriga field emission microscope. Images were acquired at an accelerating voltage of 5 kV, under a chamber pressure of approximately 4.17×10^{-6} mbar, and with working distances between 3 and 5 mm. Samples were mounted on standard SEM stubs using conductive carbon tape.

To quantitatively evaluate the morphological differences between the SbSeI samples synthesized under different conditions, a statistical analysis of the column widths was performed. For each morphology, the widths of 150 individual columns were digitally measured from representative SEM micrographs. The resulting datasets were analyzed and fitted using a lognormal distribution model. The goodness of fit was evaluated using the chi-square test implemented in Origin software, confirming that the data were well described by a lognormal distribution. The extracted distributions were then used to compare the shift in column width as a function of synthesis conditions.

PEC measurements were carried out at room temperature using a potentiostat/galvanostat (Autolab PGSTAT101 with impedance module, Metrohm) in a standard three-electrode configuration (Fig.S2) following the procedure previously reported in our earlier work [28]. The SbSeI-based device functioned as the working electrode (WE), while a Pt foil (Metrohm, 1 cm² active area) and an Ag/AgCl electrode in 3 M KCl (Metrohm) served as the counter (CE) and reference (RE) electrodes, respectively.

Measurements were conducted in 1 M phosphate buffer, prepared by mixing KH_2PO_4 and K_2HPO_4 in a 1:2 molar ratio. A neutral phosphate buffer was chosen as the main electrolyte in this study, as it represents a more sustainable and application-relevant alternative to strongly acidic media such as sulfuric acid. From a system-integration perspective, neutral electrolytes are particularly attractive for the realization of full-cell PEC devices, where photocathodes for the HER and photoanodes for OER must operate simultaneously. While acidic environments can artificially enhance photocathodes' performance by increasing proton availability, they are generally incompatible with many photoanode materials, which often exhibit improved stability and activity under near-neutral or alkaline conditions.[29] Therefore, evaluating SbSeI photocathodes in phosphate buffer provides a more realistic assessment of their potential for practical PEC water-splitting systems.[30] The three electrodes and the electrolyte were located in a 400 cm^3 quartz cuvette (Cuarzo y Vidrio). Before each experiment, freshly prepared electrolytes were purged with Ar for 20 min to remove dissolved gases and ensure a reliable correlation between the measured photocurrent densities (J) and H_2 evolution at the photocathode surface.

Simulated solar illumination was provided by a calibrated AAA-class Ossila solar simulator equipped with an LED light source and operated under standard AM 1.5G, 1 Sun conditions. The distance between the light source and the WE was fixed at 8.5 cm for all measurements. The light intensity was verified using a Thorlabs optical power meter coupled to an integrating sphere. To ensure a reproducible homogeneous illumination, the exposed WE area was restricted to approximately 1 cm², and the exact active area was determined digitally for accurate J calculations. Taking into account the 10 nA current resolution of the potentiostat and the 0.01 mm precision in area determination, J values are reported with two decimal digits, neglecting minor instrumental uncertainties.

Linear sweep voltammetry (LSV) measurements were conducted under cathodic scan conditions at a scan rate of 0.01 V/s. Chopped illumination experiments were performed using a custom-built external mechanical shutter operating with a 4 s cycle (2 s light / 2 s dark). The V_{on} was determined by selecting the first bias voltage at which a negative photocurrent was detected.

Cyclic voltammetry (CV) measurements were performed over a potential range from 1.0 to −0.4 V_{RHE} (Reference Hydrogen Electrode) for five consecutive cycles. Measurements were carried out both under illumination and in dark conditions to independently assess the influence of applied potential and light excitation.

View Article Online
DOI: 10.1039/D6TC00789A

Chronoamperometric (CA) stability tests were performed under chopped illumination at a fixed applied potential corresponding to the maximum efficiency point, as determined from the HC-STH analysis of each device.

Open-circuit photovoltage (V_{ocp}) measurements were performed by recording the potential under continuous illumination for 1 min until stabilization, followed by dark conditions until a steady-state potential was reached.

Photoelectrochemical impedance spectroscopy (PEIS) was carried out at 0 V_{RHE} over a frequency range from 10^5 to 10^{-1} Hz. The obtained impedance spectra were analyzed by fitting to an equivalent circuit model using ZView software.

Elemental analysis of the post-measurement electrolyte solutions was performed using inductively coupled plasma optical emission spectroscopy (ICP-OES, Agilent 5100) to quantify potential material dissolution from the WE during the photoelectrochemical tests.

Direct H_2 quantification was performed using a calibrated micro gas chromatograph (Micro-GC 990, Agilent) equipped with MS 5 Å, Plot U, and Stabilwax columns, and connected in-line to a H-type sealed PEC cell (DEK Research Instrumentation). A constant flow of N_2 (20 mL/min), regulated by a mass flow controller, was used as the carrier gas and continuously fed into the cell. The anodic and cathodic compartments were separated by a Nafion N-177 proton exchange membrane, ensuring selective proton transport while preventing crossover of the evolved gases in the different compartments.

To enable a consistent comparison among different devices and electrolyte environments, all measured potentials referenced to the Ag/AgCl electrode were converted to the RHE scale following the Nernst equation (Eq. 1): [28,31]

$$V_{RHE} = V_{Ag/AgCl} + E^0_{Ag/AgCl} + \frac{R \cdot T \cdot \ln(10) \cdot pH}{F} \qquad (1)$$

Where, $V_{Ag/AgCl}$ corresponds to the experimentally applied potential, $E^0_{Ag/AgCl}$ is the standard potential of the Ag/AgCl reference electrode (0.197 V), and pH denotes the acidity of the electrolyte. The universal gas constant R (8.314 J mol^{-1} K^{-1}), the working temperature T (298 K), and Faraday's constant F (96485 C mol^{-1}) were used in their standard form.

The half-cell solar to hydrogen (HC-STH) efficiency was calculated according to Eq. 2: [28,32]

$$\text{HC-STH (\%)} = \frac{J \times (V_{RHE} - V_{H^+/H_2})}{P_{sun}} * 100\% \qquad (2)$$

Where, J represents the measured photocurrent density (mA/cm²), V_{H^+/H_2} is the hydrogen reduction potential, fixed at 0 V_{RHE}, and P_{sun} is the incident simulated solar power density under AM 1.5G illumination (100 mW/cm²).

The applied bias photon-to-current efficiency (ABPE) was calculated according to Eq.3: [33]

$$\text{ABPE (\%)} = \frac{J \times (1.23 - V_{RHE})}{P_{sun}} * 100\% \qquad (3)$$

All the reported J, V_{on} and HC-STH efficiencies with their corresponding confidence intervals were obtained by averaging the J over three independent measurements for each condition, ensuring statistical reliability and reproducibility of the reported values.

Incident Photon-to-Current Efficiency (IPCE) spectra were obtained using monochromatic illumination, sequentially selecting discrete wavelengths. The irradiance of each LED was calibrated using an S120VC calibrated photodiode and a PM100D console (Thorlabs) before every measurement to ensure accurate

View Article Online
DOI: 10.1039/D6TC00789A

photon flux determination at the electrode surface. J was recorded for both bare and TiO_2-protected SbSeI photoelectrodes. IPCE values were calculated according to Eq.4: [33]

$$\text{IPCE}\ (\%) = \frac{1240\,J}{\lambda\,P} \qquad (4)$$

Where P is the calibrated LED irradiance (mW/cm^2), and λ is the illumination wavelength (nm). Measurements were performed at 0 V_{RHE} and at the applied bias corresponding to the maximum HC-STH efficiency extracted from LSV.

Results and Discussion

Firstly, the PEC performance of SbSeI absorbers with different morphologies was investigated following the setup depicted in Fig. S2. The synthesized SbSeI samples exhibited a nano/micro-columnar growth regime, which can be advantageous for PEC operation. A nanostructured morphology can increase the effective surface area, thereby enhancing the density of available catalytic sites and promoting reactant adsorption at the semiconductor–electrolyte interface. In addition, such architectures may improve light harvesting through enhanced optical path lengths. [34] However, excessively complex or densely packed nanocolumnar networks can be detrimental, as they may induce shadowing effects and hinder the efficient release of gaseous reaction products (H_2 and O_2) from the surface. Gas accumulation within the porous structure can partially block active sites and locally isolate the electrode from the electrolyte, ultimately leading to a significant reduction in device performance. To balance the competing effects between surface area and charge transport, three distinct SbSeI morphologies were investigated as an initial screening (Fig. 1a): SbSeI(1), SbSeI(2), and SbSeI(3). This approach enabled a systematic transition from smaller, compact, and densely packed columnar structures to larger, more spatially distributed column networks, while preserving the phase purity of the SbSeI absorber.

The statistical distribution of column widths is presented in Fig. 1d. A clear shift in the distribution is observed as a function of synthesis conditions, moving from predominantly wider columns (1100nm) in SbSeI(1) to significantly thinner columns (250 nm) in SbSeI(3), with SbSeI(2) exhibiting intermediate dimensions (500nm). This progressive narrowing of the column width reflects the controlled modulation of the growth kinetics during synthesis.

The three devices were characterized through LSV under chopped illumination to assess their photo-response, to identify possible parasitic photoelectrochemical processes beyond the HER, and to extract key performance parameters, including J, V_{on}, and HC-STH efficiency.

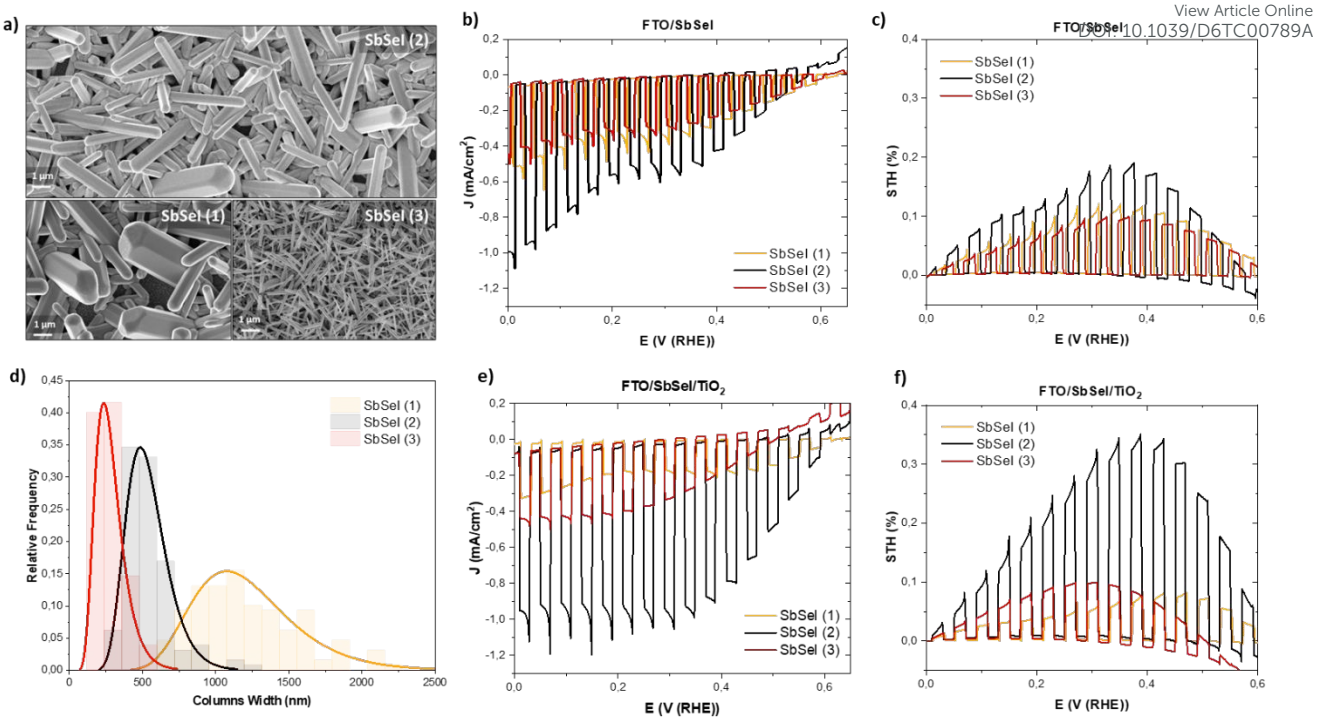

Fig. 1. Top-view scanning electron microscopy images of different morphologies of SbSeI (a). Linear sweep voltammetry under chopped illumination (b) and the corresponding half-cell solar-to-hydrogen efficiency (c) of FTO/SbSeI photocathodes. Column width distribution of the different SbSeI morphologies (d). Linear sweep voltammetry under chopped illumination (e) and the corresponding half-cell solar-to-hydrogen efficiency (f) of FTO/SbSeI/TiO_2 photocathodes.

As presented in Fig.1b, for all the devices, a similar V_{on} around 0.6 V_{RHE} was observed. This behaviour is expected, as V_{on} is primarily governed by the energetic alignment of the semiconductor with respect to the H_2 redox level.[35] Since all samples share the same material composition, stack configuration (FTO/SbSeI), and electrolyte environment (neutral phosphate buffer), the variations in morphology alone are not expected to significantly alter the band energetics or the built-in electric field responsible for initiating photogenerated charge transfer. Consequently, both the V_{on} and the overall shape of the LSV curves remain largely unchanged across the three morphologies. Nevertheless, pronounced differences are observed in J, which is strongly influenced by the interfacial properties of the absorber. As shown in Fig 1.b, SbSeI(2) reached a *J* of 1.1 mA/cm² at 0 V_{RHE} under illumination, nearly twice that obtained for SbSeI(1) and SbSeI(3), which both exhibit values around 0.6 mA/cm² at the same potential. A similar trend is reflected in the HC-STH efficiency (Fig.1c), which reaches approximately 0.2% for SbSeI(2) , compared to 0.1% for SbSeI(1) and SbSeI(3). The enhanced *J* observed for SbSeI(2) can be attributed to a more favourable balance between accessible surface area and effective electrolyte contact. While all morphologies provide nanostructured interfaces, SbSeI(2) likely maximizes the density of electrochemically active sites without introducing excessive shadowing effects or gas trapping within the columnar network. This optimized architecture facilitates more efficient charge transfer at the semiconductor–electrolyte interface and improves the extraction of photogenerated e^- for HER, thereby increasing the steady-state *J* without decreasing overpotential. Consistent with this interpretation, the maximum HC-STH occurs at similar potentials for all three devices. This indicates that the operating voltage at which optimal power conversion is achieved is mainly determined by the intrinsic photoelectrocatalytic performance of the SbSeI-based photocathode rather than by morphological variations, which instead modulate the magnitude of the J.

In all cases, a shoulder feature is observed in the LSV curves around 0.3 V_{RHE}. This feature is likely associated with competing surface processes or parasitic electrochemical reactions occurring on the uncovered SbSeI

View Article Online
DOI: 10.1039/D6TC00789A

surface, which can locally consume photogenerated carriers and reduce the effective J available for HER. The persistence of this feature across all morphologies suggests that its origin is intrinsic to the particular SbSeI–electrolyte interface under these conditions rather than morphology-specific.

To decouple morphological effects from side reaction-related phenomena, all three SbSeI photocathodes were coated with an ultrathin TiO_2 protective layer (3 nm). The introduction of this passivation layer served two main purposes: (i) to suppress direct contact between the absorber and the electrolyte, thereby mitigating surface side reactions, and (ii) to ensure that the observed differences in the photoelectrochemical performance can be attributed primarily to the SbSeI different morphology rather than to unequal side-reaction rates among the samples. After the TiO_2 deposition, SbSeI(2) exhibited again the highest PEC performance, confirming that its superior behaviour was intrinsic and not linked to undesired side redox reactions over the unprotected SbSeI surface. The V_{on} and *J* values remain essentially unchanged (Fig.1e) compared to the corresponding un-passivated devices (Fig.1b). However, the HC-STH efficiency increased from approximately 0.2% (Fig.1c) to nearly 0.4% (Fig.1f), representing an almost twofold improvement. In addition, the LSV curves of the TiO_2-protected devices displayed a noticeably cleaner profile, with the disappearance of the previously observed shoulder around 0.3 V_{RHE} for the unprotected SbSeI samples, which was associated with parasitic surface reactions. The ABPE was calculated for all devices according to Eq.3 and is reported in Fig.S3. The FTO/SbSeI/TiO_2 photocathode achieves a maximum ABPE of 1.4% at low applied bias, consistent with the superior PEC performance of SbSeI(2) identified from the HC-STH analysis. The relative ranking of the three morphologies is preserved across both metrics, further confirming that SbSeI(2) represents the optimal morphology among the tested configurations. Consequently, from this point onward, all the further studies in this work were performed on SbSeI(2) based devices (shortened to "SbSeI" in the text for simplicity) since it was the morphology that achieved the best PEC performance among the tested samples.

To further investigate the role of TiO_2 thickness, additional photocathodes were fabricated with a thicker TiO_2 overlayer (10 nm) deposited under the same low-temperature ALD conditions. Fig.S4 compares the LSV curves and HC-STH efficiencies of the bare FTO/SbSeI, FTO/SbSeI/TiO_2 (3nm) and FTO/SbSeI/TiO_2 (10nm) photocathodes. While the V_{on} remains essentially unchanged across all three configurations, a pronounced decrease in *J* and HC-STH efficiency is observed for the 10 nm TiO_2-coated device. This behaviour suggests a transition in the functional role of the TiO_2 layer as its thickness increases. At a thickness of 3 nm, TiO_2 primarily acts as a conformal protective and passivating overlayer, effectively suppressing surface changes while remaining sufficiently thin to allow an efficient charge tunneling across the SbSeI/TiO_2 interface. In contrast, a 10 nm TiO_2 layer behaves as a selective contact layer, imposing a possible additional transport barrier for photogenerated e^-.[36] Since the TiO_2 films were deposited at low temperature to prevent SbSeI decomposition, the resulting oxide is expected to be relatively resistive and to exhibit limited conductivity.[18] As a consequence, increasing the TiO_2 thickness leads to an increased resistance and reduced charge-transfer efficiency, ultimately limiting *J* and overall HC-STH. These results highlight the critical importance of TiO_2 thickness optimization in photocathodes. While ultrathin TiO_2 layers effectively improve performance and stability by passivating the absorber surface, thicker films deposited under low-temperature conditions may hinder charge transport and are therefore unsuitable without additional doping, post-deposition treatments, or alternative contact engineering strategies. Hence, 3 nm TiO_2 were selected for further analysis in this work.

To gain deeper insight into the role of TiO_2 passivation on interfacial charge-transfer processes, PEIS measurements were performed under illumination for the two representative systems: FTO/SbSeI and FTO/SbSeI/TiO_2. Fig.2a presents the corresponding Nyquist plots. The TiO_2-coated photocathode exhibits a reduced semicircle diameter compared to the bare absorber, indicating a decrease in the interfacial charge-transfer resistance and, consequently, faster charge-transfer kinetics at the semiconductor–electrolyte interface. [37] Quantitative analysis was carried out by fitting the impedance spectra using an equivalent circuit model implemented in ZView software. The extracted charge-transfer resistance values are approximately 7

View Article Online
DOI: 10.1039/D6TC00789A

kΩ for the bare FTO/SbSeI device and 6 kΩ for the TiO_2-coated photocathode. This behavior, combined with the metrics extracted from LSV, suggests that TiO_2 effectively suppresses non-radiative recombination pathways and parasitic surface reactions of the SbSeI, thereby improving charge utilization for HER rather than merely reducing resistance. These results support the use of ultrathin TiO_2 layers as an effective and environmentally benign strategy to enhance both efficiency and operational robustness without relying on aggressive or less sustainable electrolytes.

V_{ocp} analysis was conducted under light and dark conditions (Fig.2b) for both protected and unprotected devices. Upon illumination, both electrodes show a clear positive shift in potential, indicating effective photoinduced charge separation even without an external bias. However, the TiO_2-covered device achieves a higher photovoltage (0.60 V_{RHE}) compared to bare SbSeI (0.55 V_{RHE}), demonstrating enhanced interfacial quality and more efficient charge separation. Notably, the TiO_2 modified sample also maintains a higher potential in the dark, suggesting improved surface passivation and suppression of non-radiative charge loss pathways. Further insight into interfacial dynamics can be drawn from the transient response. In the unprotected electrode, a sharp dip in V_{ocp} is followed by slow recovery, linked to fast recombination and delayed charge redistribution. In contrast, the passivated sample exhibits a much smoother decay profile, consistent with reduced defect activity.

IPCE measurements were performed on both bare and TiO_2-protected SbSeI photocathodes at two applied potentials, 0 V_{RHE} and 0.4 V_{RHE} (Fig.2c). The latter was selected because both devices exhibit their maximum HC-STH efficiency at this bias, enabling a fair comparison under optimal operating conditions. At both potentials, the TiO_2-protected photocathode consistently shows higher IPCE values across the entire investigated spectral range, indicating more efficient photon-to-electron conversion upon surface passivation. For both devices, the IPCE recorded at 0 V_{RHE} was systematically higher than that measured at 0.4 V_{RHE}, in agreement with the larger *J* observed at zero bias. This behavior reflects bias-dependent charge extraction and interfacial charge-transfer kinetics rather than changes in optical absorption.[38] The IPCE spectra exhibit a pronounced response in the visible region, with a gradual decrease toward longer wavelengths. The *J* contribution drops beyond ~750 nm, consistent with the optical band gap of SbSeI (1.7 eV) (Fig S1) , confirming that the photoresponse is governed by intrinsic band-to-band absorption. At wavelengths longer than the band-gap cutoff (850–950 nm), the IPCE approaches zero for both devices, as expected for sub-band-gap excitation.[39] The residual non-zero signal observed in this region is attributed to diffuse and stray light within the measurement chamber rather than genuine photoconversion processes. Importantly, the similar spectral shape of bare and protected devices suggests that the TiO_2 overlayer does not alter the light-harvesting properties of SbSeI, while the enhanced IPCE values indicate improved charge separation efficiency and reduced surface recombination losses.[40]

To further confirm that TiO_2 passivation improves not only efficiency but also electrochemical stability under operating conditions, CV on both devices (Fig.2d and Fig.2e) were first carried out under dark conditions, followed by illumination, in order to separately assess the influence of applied bias voltage and photoexcitation. For the unprotected SbSeI photocathode, a pronounced, non-reversible peak is observed at approximately 0.3 V_{RHE}, both in the dark and under illumination. This feature is consistent with the shoulder detected in the LSV curves at the same potentials (Fig 1b) and is attributed to surface oxidation processes occurring on the bare absorber (Fig 3a). Conversely, the TiO_2-protected device does not exhibit this peak under either dark or illuminated conditions (Fig. 3e), indicating that the passivation layer effectively inhibits surface oxidation and suppresses the associated parasitic electrochemical reactions. This observation provides direct electrochemical evidence of the protective role of the TiO_2 overlayer.

CA measurements were performed (Fig.2f) on both unprotected and protected SbSeI photocathodes at a fixed applied potential corresponding to the maximum efficiency point, as determined from the HC-STH analysis. This test was used to directly assess the operational stability of the devices under continuous

View Article Online
DOI: 10.1039/D6TC00789A

photoelectrochemical operation. The unprotected SbSeI photocathode exhibits an initially stable and measurable *J*, however, the current decays after the first 10 min of operation and subsequently drops to nearly zero. This abrupt loss of activity is indicative of short-term stability followed by surface degradation, consistent with the oxide formation and parasitic reactions that will be further analyzed in Fig.3. In contrast, the TiO_2-passivated photocathode demonstrates markedly improved stability. *J* remains constant during one hour of continuous operation, retaining almost 100% of its initial value. Beyond this period, a gradual decline in *J* is observed. This substantial improvement highlights the effectiveness of the ultrathin TiO_2 layer in protecting the SbSeI absorber from rapid degradation while maintaining efficient charge transfer for HER.

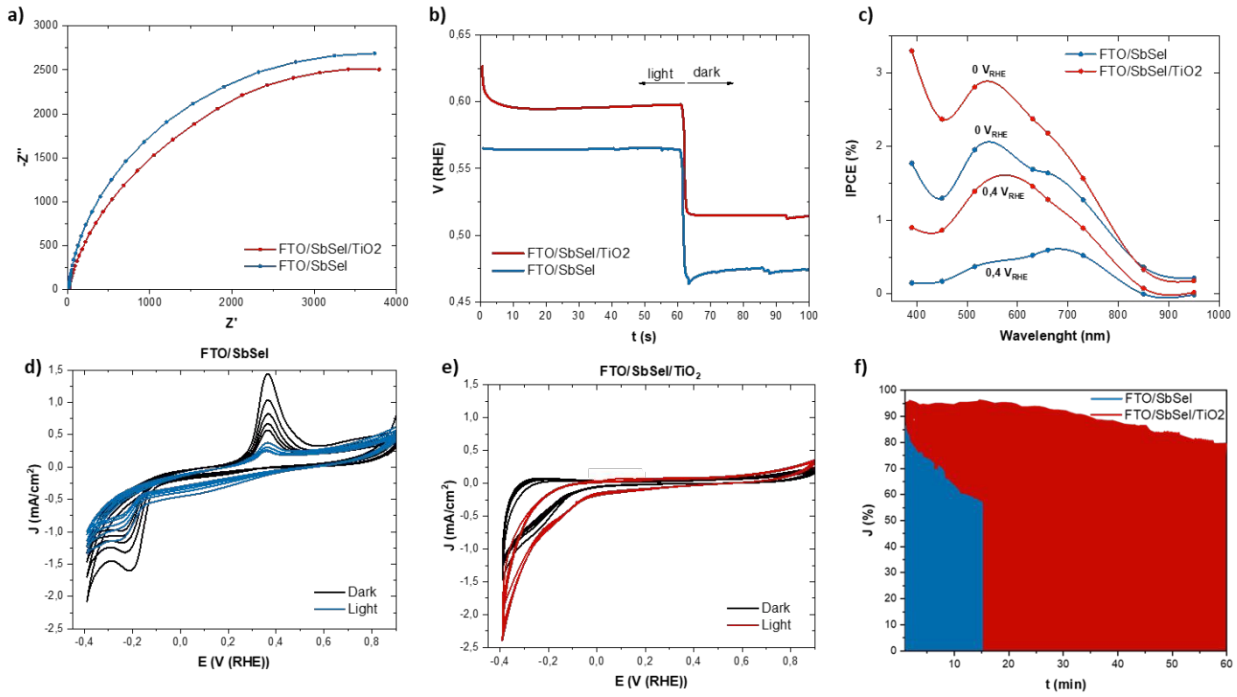

Fig. 2. Photoelectrochemical impedance spectroscopy (a), open-circuit photovoltage (b), incident photon-to-current efficiency (c) of FTO/SbSeI and FTO/SbSeI/TiO_2 photocathodes. Cyclic voltammetry of FTO/SbSeI (d) and FTO/SbSeI/TiO_2 (e) measured under both dark and illuminated conditions. Chronoamperometry (f) of FTO/SbSeI and FTO/SbSeI/TiO_2 photocathodes.

To directly measure H_2 evolution, GC measurements were conducted using a fully sealed H-type cell, in which the working and counter electrodes were physically separated into two compartments. Under PEC operation, a clear and well-defined H_2 signal was directly detected (Fig. S5), confirming H_2 production at the photocathode. This observation, together with the post-PEC structural and compositional characterization discussed below, demonstrates that the measured *J* is associated with HER rather than parasitic side reactions or capacitive processes.

To assess the structural and phase stability of the SbSeI absorber, Raman spectroscopy was performed on both protected (Fig.3a) and unprotected (Fig.3d) devices before and after PEC operation. Raman spectra collected from the fresh samples display only the characteristic vibrational modes of SbSeI, [41] with no detectable secondary phases, confirming the phase purity of the as-prepared absorbers. After PEC testing, only the Raman spectrum of the unprotected SbSeI device reveals the emergence of an additional peak at 255 cm^{-1}, which is attributed to the formation of oxide species (Sb_2O_3) at the surface.[41] This result

View Article Online
DOI: 10.1039/D6TC00789A

corroborates the electrochemical signatures observed in the CV and LSV measurements and confirms that surface oxidation occurs during PEC operation in the absence of passivation.

Notably, no corresponding changes are observed in the XRD patterns of either sample before and after PEC testing (Fig.3b and Fig.3e). In all cases, the diffraction profiles exhibit sharp, well-defined reflections consistent with crystalline SbSeI,[13,18] crystallizing in an orthorhombic cell, Pnma space group. The absence of detectable changes in XRD can be attributed to the inherently surface-sensitive nature of Raman spectroscopy compared to XRD. While Raman probes the near-surface region where oxidation occurs, XRD predominantly reflects the bulk crystallographic structure of the absorber. As a result, thin or amorphous oxide layers forming at the surface during PEC operation remain below the detection limit of XRD and do not significantly affect the bulk diffraction signal.

XPS measurements were performed on both bare (Fig. 3c) and TiO_2-protected (Fig. 3f) photocathodes before and after PEC operation to assess their chemical stability under working conditions. The survey spectra confirm that the overall elemental composition of SbSeI is preserved upon TiO_2 deposition, with characteristic Sb, Se, and I signals clearly maintained. In the protected samples, the high-resolution Ti 3s, Se 3d, I 4d, Ti 3p, and Sb 4d spectra exhibit nearly identical peak positions and line shapes before and after PEC operation, indicating that no significant chemical shifts or new chemical states are formed during operation. The Sb 4d, Se 3d, and I 4d signals remain detectable in the TiO_2-coated samples due to the finite XPS probing depth (~5–10 nm), which exceeds the TiO_2 overlayer thickness (3 nm). The reduced intensity of these peaks relative to the unprotected device is consistent with signal attenuation through the TiO_2 layer and does not indicate incomplete surface coverage.[42] These results demonstrate the chemical stability of the TiO_2-protected photocathode. In contrast, the unprotected SbSeI samples show noticeable changes in peak intensity and spectral features after PEC testing, suggesting surface modification and partial degradation under operational conditions.

Additionally, the electrolyte solutions collected after photoelectrochemical operation were analyzed by ICP-OES to evaluate possible leaching of device components during testing. For the TiO_2-protected photocathodes, no detectable elements leaks were found in the electrolyte, indicating that the ultrathin TiO_2 layer remains chemically stable under the applied operating conditions and does not undergo measurable dissolution. In contrast, electrolyte samples collected after operation of the unprotected SbSeI photocathodes exhibit detectable Sb leaching, with a measured Sb concentration of 95.68 ppb. This observation provides direct chemical evidence of absorber degradation in the absence of surface passivation and is fully consistent with the electrochemical instability and oxide formation previously identified by LSV, CV, CA and Raman spectroscopy

Together, these results demonstrate how SbSeI-based devices can be effectively utilized for stable and possibly scalable H_2 generation through water splitting.

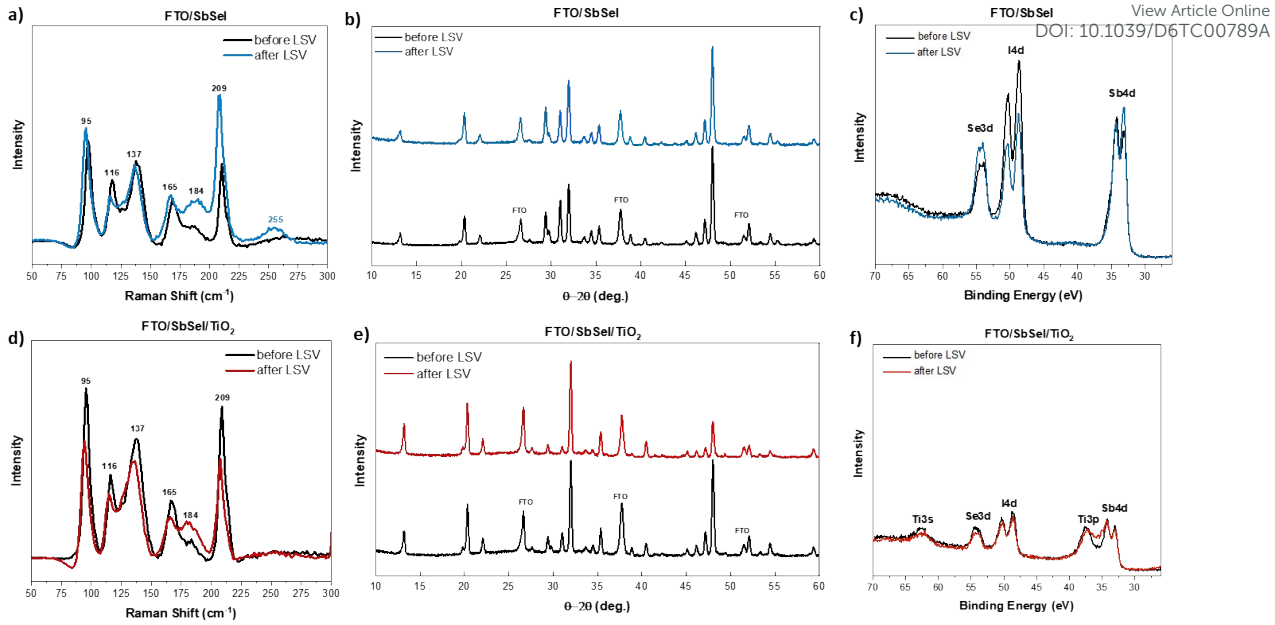

Fig. 3. Raman spectra (a), X-ray diffraction patterns (b), and X-ray photoelectron spectroscopy analysis (c) of FTO/SbSeI photocathodes before and after photoelectrochemical operation. Raman spectra (d), X-ray diffraction patterns (e), and X-ray photoelectron spectroscopy analysis (f) of FTO/SbSeI/TiO_2 photocathodes before and after photoelectrochemical operation.

Conclusions

In this work, SbSeI is demonstrated for the first time as a functional photocathode material for photoelectrochemical hydrogen evolution. By systematically investigating the effects of absorber morphology and surface passivation, it is shown how the quasi-one-dimensional structure of SbSeI can be effectively leveraged to achieve reproducible PEC activity and enhanced stability in neutral electrolyte conditions.

Morphology control is identified as a key parameter governing photocurrent density and efficiency, while the introduction of an ultrathin TiO_2 overlayer enables the decoupling of intrinsic photoelectrochemical behaviour from side reactions-related phenomena. The TiO_2 passivation layer significantly improves operational stability and suppresses parasitic surface reactions without altering the onset potential or charge collection efficiency when kept sufficiently thin, whereas thicker overlayers introduce resistive losses that limit photocurrent extraction. Through this optimized architecture, SbSeI-based photocathodes deliver a photocurrent density of 1.2 mA/cm², a half-cell solar-to-hydrogen efficiency approaching 0.4%, and sustained hydrogen evolution in neutral phosphate buffer. Importantly, these results are achieved using simple device architectures, earth-abundant materials, and environmentally benign operating conditions, without relying on scarce or noble metal nanoparticle catalysts.

This study establishes SbSeI as a promising photocathode and highlights quasi-one-dimensional chalcohalide semiconductors as a viable direction for the development of sustainable and possibly scalable photoelectrochemical hydrogen production technologies.

Author contributions

Edoardo Maggi: writing, original draft, methodology, investigation, formal analysis, conceptualization. Alejandro Navarro Guell: methodology, investigation, review. Oriol Segura-Blanch: methodology,

View Article Online
DOI: 10.1039/D6TC00789A

investigation. Ivan Caño: methodology, investigation. Lorenzo Calvo-Barrio: methodology, investigation. Lluís Soler: writing, review and editing, methodology, conceptualization, validation, resources, funding acquisition, supervision. Edgardo Saucedo: writing, review and editing, methodology, conceptualization, validation, resources, funding acquisition, supervision.

Conflicts of interest

There are no conflicts of interest to declare.

Acknowledgements

This project received funding from the European Union's H2020 ERC-Consolidator programme under grant agreement number no. 866018 (SENSATE), and by the Science and Innovation Ministry of Spain/FEDER projects number PID2023-148976OB-C41/C44 (CURIO-CITY), PID2021-124572OB-C31 (HYNTERCAT) and PCI2023-145971-2 (ACT-FAST, CET-Partnership 2023 program). The authors belong to the ''Micro and Nanotechnologies for Solar Energy Group'' (MNTSolar) and ''Energy, Catalysis, Process and Reaction Engineering'' (ENCORE) consolidated research groups of the ''Generalitat de Catalunya'' (2021 SGR 01286 and 2021 SGR 01061, respectively). This work is also part of Maria de Maeztu Units of Excellence Programme CEX2023-001300-M/funded by MICIU/AEI/ 10.13039/501100011033.O.S.B. is grateful to the Science and Innovation Ministry of Spain for the FPI fellowship no. PREP2023-001768. A.N. acknowledges the Spanish Ministry of Science and Innovation for his FPI Ph.D. grant (PRE-2021-098293. E.S. is grateful to ICREA Academia program. L.S. is grateful to the MICINN Ramon y Cajal program (grant agreement RYC2019-026704).

References

(1) Pirrone, N.; Bella, F.; Hernández, S. Solar H_2 Production Systems: Current Status and Prospective Applications. *Green Chem.* **2022**, *24* (14), 5379–5402. https://doi.org/10.1039/D2GC00292B.

(2) Kim, J. H.; Hansora, D.; Sharma, P.; Jang, J.-W.; Lee, J. S. Toward Practical Solar Hydrogen Production – an Artificial Photosynthetic Leaf-to-Farm Challenge. *Chem. Soc. Rev.* **2019**, *48* (7), 1908–1971. https://doi.org/10.1039/C8CS00699G.

(3) Fernandez-Ibanez, P.; McMichael, S.; Rioja Cabanillas, A.; Alkharabsheh, S.; Tolosana Moranchel, A.; Byrne, J. A. New Trends on Photoelectrocatalysis (PEC): Nanomaterials, Wastewater Treatment and Hydrogen Generation. *Curr. Opin. Chem. Eng.* **2021**, *34*, 100725. https://doi.org/10.1016/j.coche.2021.100725.

(4) Vilanova, A.; Dias, P.; Lopes, T.; Mendes, A. The Route for Commercial Photoelectrochemical Water Splitting: A Review of Large-Area Devices and Key Upscaling Challenges. *Chem. Soc. Rev.* **2024**, *53* (5), 2388–2434. https://doi.org/10.1039/D1CS01069G.

(5) Bora, L. V.; Bora, N. V. Photoelectrocatalytic Water Splitting for Efficient Hydrogen Production: A Strategic Review. *Fuel* **2025**, *381*, 133642. https://doi.org/10.1016/j.fuel.2024.133642.

(6) Idriss, H.; Scott, M.; Subramani, V. Introduction to Hydrogen and Its Properties. In *Compendium of Hydrogen Energy*; Elsevier, 2015; pp 3–19. https://doi.org/10.1016/B978-1-78242-361-4.00001-7.

(7) Nishioka, S.; Osterloh, F. E.; Wang, X.; Mallouk, T. E.; Maeda, K. Photocatalytic Water Splitting. *Nat. Rev. Methods Primer* **2023**, *3* (1), 42. https://doi.org/10.1038/s43586-023-00226-x.

View Article Online
DOI: 10.1039/D6TC00789A

(8) Fang, W.; Chen, S.; Jin, K.; Liu, C. Computational Study Reveals the Exceptional Photocatalytic Water Splitting Performance of Two-Dimensional Janus Kagome Lattice Nb3TeCl7. *Int. J. Hydrog. Energy* **2025**, *129*, 291–296. https://doi.org/10.1016/j.ijhydene.2025.04.309.

(9) Mamun, A. A.; Billah, A.; Anisuzzaman Talukder, M. Effects of Activation Overpotential in Photoelectrochemical Cells Considering Electrical and Optical Configurations. *Heliyon* **2023**, *9* (6), e17191. https://doi.org/10.1016/j.heliyon.2023.e17191.

(10) Ghorpade, U. V.; Suryawanshi, M. P.; Green, M. A.; Wu, T.; Hao, X.; Ryan, K. M. Emerging Chalcohalide Materials for Energy Applications. *Chem. Rev.* **2023**, *123* (1), 327–378. https://doi.org/10.1021/acs.chemrev.2c00422.

(11) Zhang, H.; Xia, Y.; Zhang, Y.; Ghorpade, U. V.; He, M.; Shin, S. W.; Hao, X.; Suryawanshi, M. P. The Rise of Chalcohalide Solar Cells: Comprehensive Insights From Materials to Devices. *Adv. Sci.* **2025**, *12* (19), 2413131. https://doi.org/10.1002/advs.202413131.

(12) Caño-Prades, I.; Navarro-Güell, A.; Giraldo, S.; Puigdollers, J.; Placidi, M.; Saucedo, E. Novel 1D van Der Waals SbSeI Micro-Columnar Solar Cells by a Self-Catalyzed High Pressure Process. In *2022 IEEE 49th Photovoltaics Specialists Conference (PVSC)*; IEEE: Philadelphia, PA, USA, 2022; pp 1304–1304. https://doi.org/10.1109/PVSC48317.2022.9938875.

(13) Caño, I.; Navarro-Güell, A.; Maggi, E.; Gon Medaille, A.; Rovira, D.; Jimenez-Arguijo, A.; Segura, O.; Torrens, A.; Jimenez, M.; López, C.; Benítez, P.; Cazorla, C.; Jehl, Z.; Gong, Y.; Asensi, J.; Calvo-Barrio, L.; Soler, L.; Llorca, J.; Tamarit, J.; Galiana, B.; Dimitrievska, M.; Ruiz-Marín, N.; Chun, H. Z.; Wong, L.; Puigdollers, J.; Placidi, M.; Saucedo, E. Ribbons of Light: Emerging (Sb,Bi)(S,Se)(Br,I) Van Der Waals Chalcohalides for Next-Generation Energy Applications. *Small* **2025**, *21* (37), e05430. https://doi.org/10.1002/smll.202505430.

(14) Ghorpade, U. V.; Suryawanshi, M. P.; Green, M. A.; Wu, T.; Hao, X.; Ryan, K. M. Emerging Chalcohalide Materials for Energy Applications. *Chem. Rev.* **2023**, *123* (1), 327–378. https://doi.org/10.1021/acs.chemrev.2c00422.

(15) Leontyeva, X. A.; Ivanova, N. A.; Khussurova, G. M.; Puzikova, D. S.; Galeyeva, A. K. Photoelectrochemical Performance of BiSI/Bi_{13} S_{18} I_2 Thin Films Prepared via One-Step Chemical Bath Deposition. *Electroanalysis* **2025**, *37* (11), e70079. https://doi.org/10.1002/elan.70079.

(16) Chauhan, P.; Singh, J.; Kumar, A. Two-Dimensional Janus Antimony Chalcohalides for Efficient Energy Conversion Applications. *J. Mater. Chem. A* **2024**, *12* (26), 16129–16142. https://doi.org/10.1039/D4TA02974G.

(17) Nie, R.; Hu, M.; Risqi, A. M.; Li, Z.; Seok, S. I. Efficient and Stable Antimony Selenoiodide Solar Cells. *Adv. Sci.* **2021**, *8* (8), 2003172. https://doi.org/10.1002/advs.202003172.

(18) Caño, I.; Navarro-Güell, A.; Maggi, E.; Barrio, M.; Tamarit, J.-L.; Svatek, S.; Antolín, E.; Yan, S.; Barrena, E.; Galiana, B.; Placidi, M.; Puigdollers, J.; Saucedo, E. SbSeI and SbSeBr Micro-Columnar Solar Cells by a Novel High Pressure-Based Synthesis Process. *J. Mater. Chem. A* **2023**, *11* (33), 17616–17627. https://doi.org/10.1039/D3TA03179A.

(19) Jeon, J.; Kang, J.; Zhang, X.; Choi, K. H.; Jeong, B. J.; Woo, C.; Dong, X.; Kim, S. H.; Park, J.-H.; Baik, J. M.; Oh, H.-S.; Yu, H. K.; Choi, J.-Y. Chalcogen Alloying for Band Structure Modulation of Antimony Chalcogen Iodide Alloy: 1D van Der Waals Materials SbSI–SbSeI System. *CrystEngComm* **2024**, *26* (6), 817–821. https://doi.org/10.1039/D3CE00998J.

(20) Cheng, J.; Wang, W.; An, C.; Wang, L.; Yang, J.; Yin, Y.; Zhou, W.; Peng, Y.; Tang, D. Quasi-1D SbSeI for a High-Performance near-Infrared Polarization-Sensitive Photodetector. *Appl. Phys. Lett.* **2024**, *124* (10), 102101. https://doi.org/10.1063/5.0191682.

(21) Song, H.; Luo, S.; Huang, H.; Deng, B.; Ye, J. Solar-Driven Hydrogen Production: Recent Advances, Challenges, and Future Perspectives. *ACS Energy Lett.* **2022**, *7* (3), 1043–1065. https://doi.org/10.1021/acsenergylett.1c02591.

(22) Asha, K.; Satsangi, V. R.; Shrivastav, R.; Kant, R.; Dass, S. Effect of Morphology and Impact of the Electrode/Electrolyte Interface on the PEC Response of Fe_2 O_3 Based Systems – Comparison of Two Preparation Techniques. *RSC Adv.* **2020**, *10* (69), 42256–42266. https://doi.org/10.1039/D0RA07870K.

(23) Kubacka, A.; Fernández-García, M.; Colón, G. Advanced Nanoarchitectures for Solar Photocatalytic Applications. *Chem. Rev.* **2012**, *112* (3), 1555–1614. https://doi.org/10.1021/cr100454n.

(24) Cui, W.; Moehl, T.; Siol, S.; Tilley, S. D. *Operando* Electrochemical Study of Charge Carrier Processes in Water Splitting Photoanodes Protected by Atomic Layer Deposited TiO_2. *Sustain. Energy Fuels* **2019**, *3* (11), 3085–3092. https://doi.org/10.1039/C9SE00399A.

(25) Capitão, J.; Da Silva Lopes, T.; Rodrigues, L.; Lopes, T.; Dias, P.; Ivanou, D.; Mendes, A. Enhancing Large-Area Photoelectrochemical Cells' Performance through Conductivity Improvement of Customizable FTO Collectors Grid. *J. Power Sources* **2025**, *654*, 237788. https://doi.org/10.1016/j.jpowsour.2025.237788.

(26) Lam, N. H.; Nguyen Truong, N. T.; Kim, C.-D.; Shaikh, H.; Tamboli, M. S.; Alam, M. A.; Jung, J. H. Elevating Photoelectrochemical Water Splitting Efficiency Using Synergistic CuO@ZBO Photocathode. *Int. J. Hydrog. Energy* **2024**, *110*, 359–370. https://doi.org/10.1016/j.ijhydene.2025.02.228.

(27) Alejandro Navarro Güell. Syntesis and Morphology Control of SbSeI Thin Fims at Elevated Pressure. https://doi.org/10.1039/d6ma00048g.

(28) Maggi, E.; Segura-Blanch, O.; Caño, I.; Torrens, A.; Jimenez-Arguijo, A.; Estarlich, P.; Calvo-Barrio, L.; Chun, H. Z.; Garcia-Sanchez, M. F.; Placidi, M.; Puigdollers, J.; Llorca, J.; Wong, L. H.; Soler, L.; Saucedo, E. Minimalist and Nanoparticle-Free Selenium-Based Photocathodes for Record Performance Solar-Driven Hydrogen Evolution. *EES Catal.* **2026**, 10.1039.D5EY00297D. https://doi.org/10.1039/D5EY00297D.

(29) Chatenet, M.; Pollet, B. G.; Dekel, D. R.; Dionigi, F.; Deseure, J.; Millet, P.; Braatz, R. D.; Bazant, M. Z.; Eikerling, M.; Staffell, I.; Balcombe, P.; Shao-Horn, Y.; Schäfer, H. Water Electrolysis: From Textbook Knowledge to the Latest Scientific Strategies and Industrial Developments. *Chem. Soc. Rev.* **2022**, *51* (11), 4583–4762. https://doi.org/10.1039/D0CS01079K.

(30) Kageshima, Y.; Kumagai, H.; Teshima, K.; Domen, K.; Nishikiori, H. Neutral Buffered Electrolytes Guarantee Ideal Band-Edge Pinning for Semiconductor Photoanodes. *Chem. Sci.* **2025**, *16* (31), 14088–14097. https://doi.org/10.1039/D5SC01816A.

(31) Higashi, T.; Kaneko, H.; Minegishi, T.; Kobayashi, H.; Zhong, M.; Kuang, Y.; Hisatomi, T.; Katayama, M.; Takata, T.; Nishiyama, H.; Yamada, T.; Domen, K. Overall Water Splitting by Photoelectrochemical Cells Consisting of $(ZnSe)_{0.85}$ $(CuIn_{0.7}$ $Ga_{0.3}$ Se_2 $)_{0.15}$ Photocathodes and $BiVO_4$ Photoanodes. *Chem Commun* **2017**, *53* (85), 11674–11677. https://doi.org/10.1039/C7CC06637F.

(32) Huang, D.; Wang, K.; Li, L.; Feng, K.; An, N.; Ikeda, S.; Kuang, Y.; Ng, Y.; Jiang, F. 3.17% Efficient Cu_2 $ZnSnS_4$ –$BiVO_4$ Integrated Tandem Cell for Standalone Overall Solar Water Splitting. *Energy Environ. Sci.* **2021**, *14* (3), 1480–1489. https://doi.org/10.1039/D0EE03892J.

(33) Chen, Z.; Jaramillo, T. F.; Deutsch, T. G.; Kleiman-Shwarsctein, A.; Forman, A. J.; Gaillard, N.; Garland, R.; Takanabe, K.; Heske, C.; Sunkara, M.; McFarland, E. W.; Domen, K.; Miller, E. L.; Turner, J. A.; Dinh, H. N. Accelerating Materials Development for Photoelectrochemical Hydrogen Production: Standards for Methods, Definitions, and Reporting Protocols. *J. Mater. Res.* **2010**, *25* (1), 3–16. https://doi.org/10.1557/JMR.2010.0020.

(34) Shim, S. G.; Tan, J.; Lee, H.; Park, J.; Yun, J.; Park, Y. S.; Kim, K.; Lee, J.; Moon, J. Facile Morphology Control Strategy to Enhance Charge Separation Efficiency of Mo:BiVO4 Photoanodes for Efficient Photoelectrochemical Water Splitting. *Chem. Eng. J.* **2022**, *430*, 133061. https://doi.org/10.1016/j.cej.2021.133061.

(35) Serpone, N.; Emeline, A. V.; Ryabchuk, V. K.; Kuznetsov, V. N.; Artem'ev, Y. M.; Horikoshi, S. Why Do Hydrogen and Oxygen Yields from Semiconductor-Based Photocatalyzed Water Splitting Remain Disappointingly Low? Intrinsic and Extrinsic Factors Impacting Surface Redox Reactions. *ACS Energy Lett.* **2016**, *1* (5), 931–948. https://doi.org/10.1021/acsenergylett.6b00391.

(36) Shi, J.; Zhao, X.; Li, C. Surface Passivation Engineering for Photoelectrochemical Water Splitting. *Catalysts* **2023**, *13* (2), 217. https://doi.org/10.3390/catal13020217.

(37) Delgado, A.; García-Sánchez, M. F.; M'Peko, J.-C.; Ruiz-Salvador, A. R.; Rodríguez-Gattorno, G.; Echevarría, Y.; Fernández-Gutierrez, F. An Elementary Picture of Dielectric Spectroscopy in Solids: Physical Basis. *J. Chem. Educ.* **2003**, *80* (9), 1062. https://doi.org/10.1021/ed080p1062.

(38) Guler, A. C.; Antos, J.; Masar, M.; Urbanek, M.; Machovsky, M.; Kuritka, I. Comprehensive Evaluation of Photoelectrochemical Performance Dependence on Geometric Features of ZnO Nanorod Electrodes. *Nanoscale Adv.* **2023**, *5* (11), 3091–3103. https://doi.org/10.1039/D3NA00089C.

(39) Alqahtani, M.; Sathasivam, S.; Chen, L.; Jurczak, P.; Piron, R.; Levallois, C.; Létoublon, A.; Léger, Y.; Boyer-Richard, S.; Bertru, N.; Jancu, J.; Cornet, C.; Wu, J.; Parkin, I. P. Photoelectrochemical Water Oxidation of $GaP_{1-x}Sb_x$ with a Direct Band Gap of 1.65 eV for Full Spectrum Solar Energy Harvesting. *Sustain. Energy Fuels* **2019**, *3* (7), 1720–1729. https://doi.org/10.1039/C9SE00113A.

(40) Hwang, Y. J.; Hahn, C.; Liu, B.; Yang, P. Photoelectrochemical Properties of TiO_2 Nanowire Arrays: A Study of the Dependence on Length and Atomic Layer Deposition Coating. *ACS Nano* **2012**, *6* (6), 5060–5069. https://doi.org/10.1021/nn300679d.

(41) Dolcet Sadurni, M.; Timmo, K.; Mikli, V.; Volobujeva, O.; Mengü, I.; Krustok, J.; Grossberg-Kuusk, M.; Kauk-Kuusik, M. Preparation and Characterization of SbSeI Thin Films. *J. Sci. Adv. Mater. Devices* **2024**, *9* (1), 100664. https://doi.org/10.1016/j.jsamd.2023.100664.

(42) Jablonski, A. Evaluation of Procedures for Overlayer Thickness Determination from XPS Intensities. *Surf. Sci.* **2019**, *688*, 14–24. https://doi.org/10.1016/j.susc.2019.05.004.

View Article Online
DOI: 10.1039/D6TC00789A

Data availability

All raw data supporting the findings of this study, are available in the Zenodo repository at https://doi.org/10.5281/zenodo.18458021